Chemical Engineering Journal 545 (2026) 179707

Contents lists available at ScienceDirect

Chemical Engineering Journal

journal homepage: www.elsevier.com/locate/cej

Engineering a covalent S-scheme heterojunction in TpBpy/MIL-68(In) to boost interfacial charge transfer for efficient solar-to-hydrogen conversion

Yuying Hu, Huihui Zhang, Jiayi Meng, Yifan Liao, Yuchen Wei, Quanmei Zhou, Mohan Zhang, Yamei Huang, Wei-Lin Dai *

State Key Laboratory of Porous Materials for Separation and Conversion, Shanghai Key Laboratory of Molecular Catalysis and Innovative Materials, Department of Chemistry, Fudan University, Shanghai, 200438, PR China

ARTICLE INFO

Keywords:
TpBpy covalent organic framework
MIL-68 metal organic framework
Covalent integration
S-scheme heterojunction
Photocatalytic hydrogen evolution

ABSTRACT

Engineering high-efficiency S-scheme heterojunctions with robust interfacial charge transfer channels is critical for simultaneously achieving spatial charge separation and preserving the strong redox potential of photogenerated carriers. Herein, we report the successful construction of a novel covalently integrated TpBpy/MIL-68(In) S-scheme heterostructure via an in situ solvothermal strategy. Uniquely, MIL-68(In) nanorods function as dynamic quasi-templates, in which partial structural dissolution orchestrates an in situ self-etching process to guide the epitaxial growth of TpBpy via Schiff-base condensation. This dynamic evolution transforms simple two-dimensional physical contact into a three-dimensionally interlocked covalent interface, thereby maximizing the effective contact area. The optimized covalently integrated heterostructure exhibits an enhanced photocatalytic hydrogen evolution rate of 13.7 mmol g^{-1} h^{-1} under simulated sunlight, representing a remarkable enhancement of 68.5-fold and 1.9-fold compared to pristine MIL-68(In) and TpBpy, respectively. Furthermore, combined in situ irradiated XPS and DFT calculations provide direct evidence for the interfacial electron cloud redistribution induced by chemical bonds. These robust covalent bridges establish a strong built-in electric field (IEF) and continuous low-impedance channels, effectively circumventing the high contact resistance and severe charge recombination typical of physically mixed systems. This work provides a meaningful paradigm for the interfacial engineering of metal-organic framework (MOF)/covalent organic framework (COF) based covalent heterojunctions to achieve advanced solar-to-hydrogen conversion.

1. Introduction

The exploration of clean and renewable energy alternatives has become a global imperative [1,2], primarily driven by the rapid exhaustion of conventional fossil fuels and the escalating crisis of environmental degradation [3]. Characterized by a high energy density, zero carbon emissions, and infinite renewability, hydrogen (H_2) is widely recognized as the ideal secondary energy carrier of the 21st century [4,5]. Among various energy conversion pathways, solar-driven photocatalytic water splitting over semiconductor materials is regarded as a highly promising frontier technology, as it enables the direct conversion of ubiquitous solar energy into high-energy-density green hydrogen [6,7].

In recent years, porous crystalline materials such as metal-organic frameworks (MOFs) [8–10] and covalent organic frameworks (COFs) [11–13] have exhibited broad application prospects in the field of photocatalysis due to their advantages, including ultrahigh specific surface areas, highly customizable pore structures, and facile molecular-level functionalization. Specifically, MOFs represent a distinct family of well-ordered porous networks formulated via the coordinate bonds connecting metal centers with organic bridging units, possessing favorable optical responsivity, abundant metal active sites and tunable pore structures [14]. However, when pristine MOFs are utilized for the photocatalytic water splitting reaction, they generally suffer from relatively poor photocatalytic hydrogen evolution activity and stability, which are primarily attributed to their structural instability and the severe recombination of photogenerated charge carriers [15]. The photocatalytic efficiency of MOF-based platforms can be substantially amplified through the rational design of heterojunctions, which involves hybridizing MOFs with diverse active materials, as exemplified by TiO_2@Ti MOFs [16], Zr MOFs@$ZnIn_2S_4$ [17], Ni-MOFs/$ZnIn_2S_4$ [18], and ZIF-67@Ni-Fe LDH [19], which further demonstrates the great

* Corresponding author.
E-mail address: wldai@fudan.edu.cn (W.-L. Dai).

https://doi.org/10.1016/j.cej.2026.179707
Received 9 May 2026; Received in revised form 16 July 2026; Accepted 18 July 2026
Available online 20 July 2026

potential of MOF materials in photocatalysis. Similar to MOFs, COFs are another class of porous materials with excellent properties, constructed by linking organic ligands via reversible covalent bonds. They have attracted considerable attention owing to their narrow bandgaps, superior optical responsivity, and large specific surface areas [20–22]. Nevertheless, the intrinsic drawbacks of COF materials, such as poor electrical conductivity and a lack of metal active sites, inevitably limit their photocatalytic reactivity. Constructing heterojunctions is a crucial approach to enhancing the catalytic activity of COFs. Compared to the majority of previous works that rely on the surface modification of inorganic semiconductors to form organic-inorganic heterojunctions with COFs [23,24], utilizing the inherently abundant surface functional groups of MOFs to directly integrate them with COFs via covalent bonds holds great promise. This strategy can generate strong interfacial interactions and establish rapid electron transfer channels, thereby constructing highly efficient composite semiconductor photocatalysts [25]. The S-scheme configuration, unlike classic Type-II heterojunctions [26,27], transcends traditional limitations by not only substantially enhancing the spatial decoupling of photogenerated charge carriers [28–30], but also effectively preserving the strongly reductive and oxidative band potentials of the catalysts, thereby realizing highly efficient surface catalytic reactions [31,32]. In contrast to physically mixed composites, a covalently integrated heterostructure achieved through strong interfacial chemical bonds can provide highly robust interfacial contact. More importantly, the construction of covalent linkages at the molecular scale acts as a continuous, low-impedance bridge for charge migration, which establishes rapid electron transfer channels and significantly suppresses charge recombination. Consequently, this covalent integration strategy is expected to yield highly efficient semiconductor photocatalysts with significantly enhanced solar-to-energy conversion capabilities [33,34].

In this work, a novel covalently integrated TpBpy/MIL-68(In) S-scheme heterostructure was successfully constructed via an in situ solvothermal strategy. Crucially, MIL-68(In) nanorods function as a dynamic quasi-template; their partial dissolution facilitates an in situ self-etching process that guides the growth of TpBpy through Schiff-base condensation. This leads to a unique interlocked interface with maximized contact area and minimized transfer resistance. The optimized heterostructure achieved a photocatalytic hydrogen evolution (PHE) rate of 13.7 mmol g^{-1} h^{-1}, significantly outperforming its individual components. Comprehensive analysis via in situ irradiated XPS and density functional theory (DFT) calculations provide proof of the continuous interfacial electron cloud redistribution, establishing a robust IEF and S-scheme pathways. Thus, covalently integrated TpBpy/MIL-68(In) composite is capable of high and stable hydrogen evolution performance.

2. Experimental

2.1. Preparation of MIL-68(in) nanorods

The MIL-68(In) nanorods were synthesized via a solvothermal method. Briefly, 1.5 mL of *N*,*N*-dimethylformamide (DMF), 46 mg of 2-aminoterephthalic acid, 8 mg of benzoic acid, and 40 μL of pyridine were sequentially added into a 50 mL Teflon liner of an autoclave. Meanwhile, 134 mg of $In(NO_3)_3{\cdot}4.5H_2O$ was dispersed in 10 mL of DMF. Subsequently, the dispersion was added dropwise into the Teflon liner. After 5 min of ultrasonic treatment, the autoclave was transferred to an oven and maintained at 125 °C. After cooling to room temperature naturally, the resulting yellow precipitate was collected by centrifugation, washed multiple times with DMF and anhydrous ethanol sequentially, and finally dried at 60 °C overnight to obtain the MIL-68(In) nanorods.

2.2. Preparation of TpBpy/MIL-68(in) composites

The TpBpy/MIL-68(In) composites were constructed via an in situ solvothermal strategy based on MIL-68(In) precursors. Initially, a 10 mL Pyrex glass vessel was loaded with a predetermined weight of MIL-68 (In), 31.5 mg of 1,3,5-triformylphloroglucinol (Tp), and 41.9 mg of 5,5′-diamino-2,2′-bipyridine (Bpy). A solvent mixture comprising 2.4 mL of *N*,*N*-dimethylacetamide (DMAc) and 0.8 mL of 1,2-dichlorobenzene (o-DCB) was then introduced dropwise. Following a 5-min ultrasonic treatment to obtain a homogeneous suspension, 0.3 mL of acetic acid (6 M) was added to initiate the Schiff-base reaction. The reaction mixture was fully degassed using three freeze-pump-thaw cycles, sealed under a vacuum atmosphere, and subsequently maintained at 120 °C for a duration of 72 h. Upon completion, the vessel was cooled to room temperature naturally. The obtained dark red solid underwent a sequential washing process involving DMAc, dichloromethane (DCM), and acetone (thrice for each solvent). Afterwards, the material was dried under vacuum conditions at 150 °C for a duration of 12 h, yielding the target TpBpy/MIL-68(In) composites. During the experiment, composites with different mass fractions of MIL-68(In) (5%, 10%, 20%, 30%, and 40%) were synthesized by adjusting the added amount of the MIL-68(In) precursor to 2.5 mg, 5.0 mg, 10.0 mg, 15.0 mg, and 20.0 mg, respectively. Concurrently, pristine TpBpy was prepared following the identical procedure, except for the absence of the MIL-68(In) precursor.

2.3. Preparation of control samples

In-doped TpBpy was synthesized as a control material via the following procedure: 50 mg of TpBpy was added into 100 mL of ethanol and sonicated for 10 min to achieve complete dispersion. Subsequently, 1.3 mg of $In(NO_3)_3{\cdot}4.5H_2O$ was introduced into the suspension. The resulting mixture underwent continuous stirring for 24 h under ambient conditions. Upon completion, the obtained solid was purified via repeated ethanol washings, isolated by centrifugation, and vacuum-dried at 150 °C for 12 h to obtain the In-doped TpBpy, which was denoted as 0.64%In/TpBpy. Furthermore, a sample prepared by mechanically stirring MIL-68(In) and TpBpy was denoted as M-TpBpy/20% MIL-68(In).

2.4. Characterization and theoretical method

The apparatus for the characterization and the computational details can be found in the Supporting Information.

3. Results and discussion

3.1. Morphology and structure characterization

The synthetic route of the TpBpy/MIL-68(In) composite photocatalyst is schematically illustrated in Fig. 1. Initially, MIL-68(In) nanorods were synthesized via a solvothermal method to serve as the precursor. Subsequently, an in situ solvothermal strategy was employed to grow the TpBpy on the surface of the MIL-68(In) nanorods via a Schiff-base condensation reaction between the Tp and Bpy ligands, thereby preparing the covalently integrated TpBpy/MIL-68(In) composite catalyst.

To observe the surface morphologies and internal microstructural properties of the catalysts, SEM and FE-TEM analyses were utilized. As illustrated in Fig. S1 and Fig. 2a, MIL-68(In) exhibits a regular hexagonal prismatic nanorod morphology with an average lateral dimension of approximately 500 nm. Fig. 2b-c reveal that TpBpy presents an agglomerated filamentous structure. In the enlarged FE-TEM image, the red hexagon clearly shows the distorted hexagonal pore channels within TpBpy with a diameter of approximately 2 nm, verifying the successful synthesis of TpBpy. As shown in Fig. 2d and Fig. S2, the TpBpy/20%MIL-68(In) composite distinctly retains the nanorod-like skeleton of the

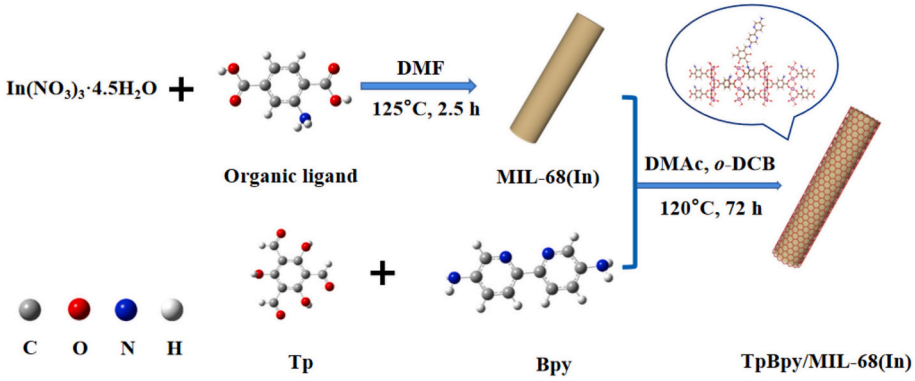

Fig. 1. Schematic illustration for the preparation of the TpBpy/MIL-68(In) heterostructure.

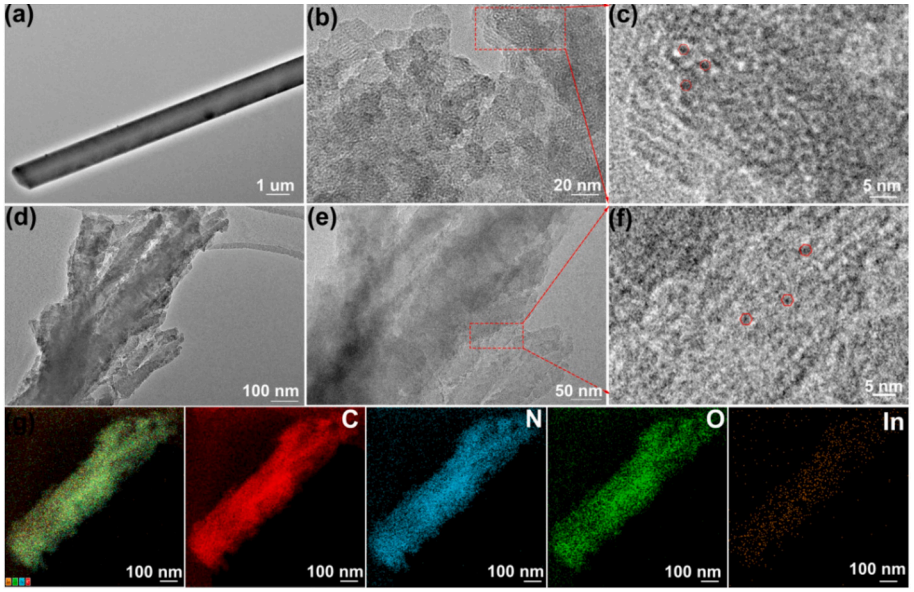

Fig. 2. (a) TEM morphology of MIL-68(In); (b) FE-TEM and (c) corresponding magnified views of TpBpy (The part circled in red is the distorted hexagonal passage); (d) FE-TEM and (e–f) high-magnification images of the TpBpy/20%MIL-68(In) composite; (g) HAADF-STEM image and the related EDS elemental mappings (C, N, O, and In) for TpBpy/20%MIL-68(In).

precursor. However, its entire surface becomes noticeably rough and densely decorated by the TpBpy layers, confirming the successful macroscopic integration of the two phases. Furthermore, magnified FE-TEM observations (Fig. 2e-f and Fig. S3) reveal a twisted hexagonal pore structure within this decorated rough surface, which clearly indicates the presence of TpBpy in the composite. The TpBpy is seamlessly integrated and densely surrounded by the adjacent matrix phases. Concurrently, Fig. 2g demonstrates that the In element is uniformly distributed throughout the composite at a relatively low concentration. Based on the above results, it can be deduced that the MIL-68(In) nanorods act as a dynamic quasi-template. Owing to the presence of amino functional groups on their surface, they undergo a Schiff-base condensation with the aldehyde ligand Tp of TpBpy, thereby covalently integrating with TpBpy to form the composite. The absence of distinct MIL-68(In) structures in the electron microscopy images can also be attributed to its structural dissolution during the synthetic reaction, resulting in its low content within the composite. Compared to simple physical mixing, this dynamic quasi-template strategy offers distinct structural and electronic advantages. Conventional methods typically rely on weak physical interactions (e.g., van der Waals forces), which inevitably lead to high interfacial contact resistance, poor phase matching, and sluggish charge transfer [35]. During the synthesis in this work, the localized partial dissolution of MIL-68(In) continuously exposes fresh uncoordinated metal sites and internal amino functional groups. These active sites act as abundant high-density anchoring points, guiding the epitaxial growth of TpBpy and facilitating the formation of robust covalent linkages between the MOF and COF phases. This dynamic process creates a three-dimensionally interlocked rough interface that maximizes the effective contact area and simultaneously establishes continuous, low-impedance channels at the molecular level, thereby fundamentally enhancing interfacial adhesion and boosting the spatial separation efficiency of photogenerated carriers [21,26].

To investigate the dynamic evolution of the precursor during the synthetic process, TpBpy/20%MIL-68(In) composite catalysts were prepared at varying reaction times and subjected to morphological characterization. With the results depicted in Fig. S4, as the synthesis proceeds from 24 h to 48 h, the MIL-68(In) nanorods undergo progressive structural dissolution and become substantially thinner. Rather than simple structural degradation, this dynamic behavior provides solid evidence for the in situ self-etching and surface reconstruction process, a strategy that echoes the self-sacrificial template concepts reported in advanced MOF-based heterojunctions [36,37].

To evaluate the crystallographic properties of the catalysts, XRD measurements were conducted. As illustrated in Fig. S5, the distinct diffraction pattern confirms the successful preparation of pristine MIL-68(In) with high crystallinity. In Fig. 3a, the XRD diffraction peaks of

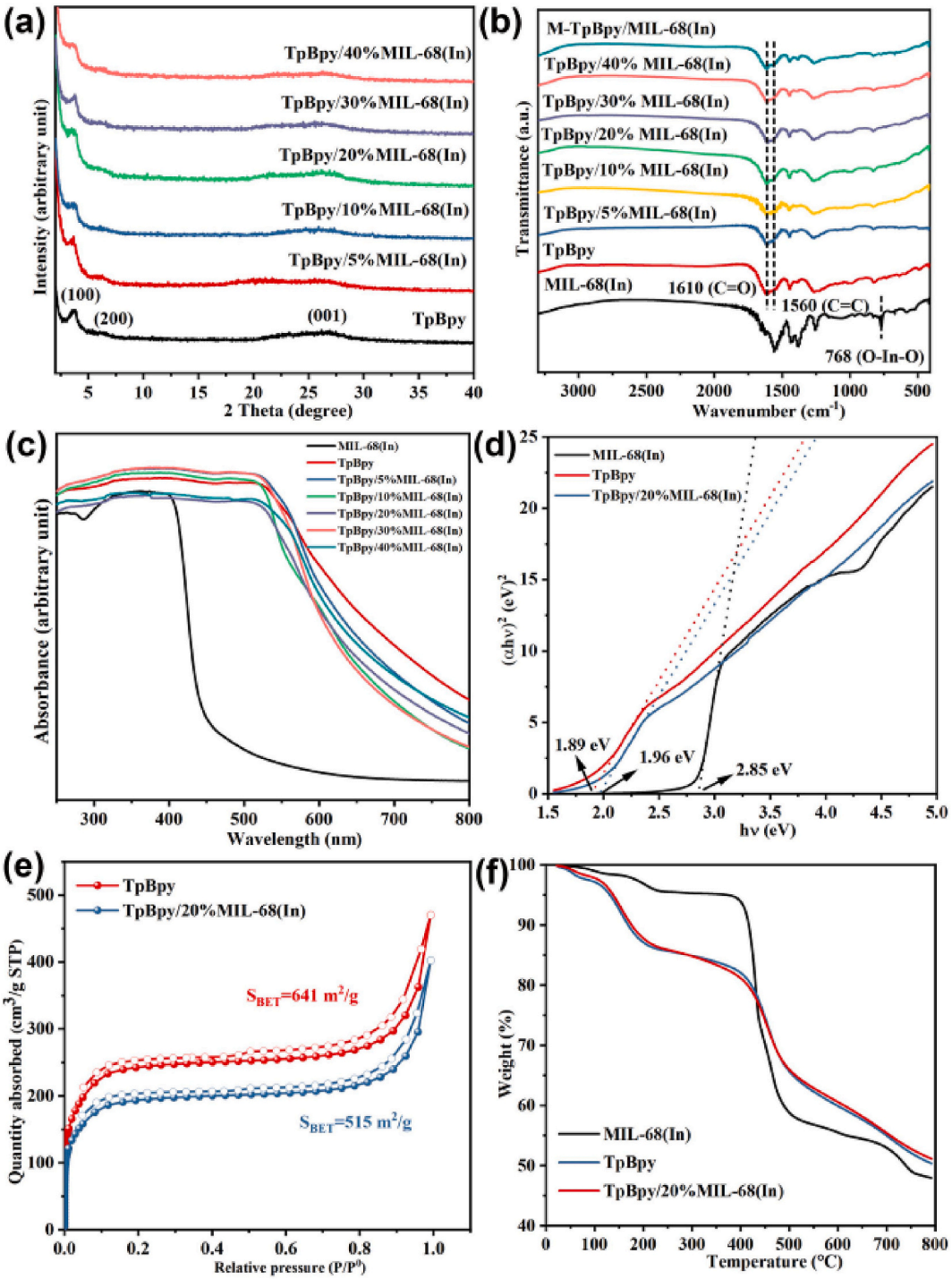

Fig. 3. (a) XRD patterns of TpBpy and TpBpy/MIL-68(In) composites, (b) FTIR spectra of the TpBpy/MIL-68(In) system, (c) UV–Vis DRS spectra of the TpBpy/MIL-68 (In) system, (d) Tauc plots of catalysts, (e) N_2 adsorption-desorption curves of TpBpy and TpBpy/20% MIL-68(In), and (f) the thermogravimetric curve of the TpBpy/ MIL-68(In) system.

the TpBpy/MIL-68(In) composite catalysts are almost identical to those of pristine TpBpy, and no diffraction peaks corresponding to MIL-68(In) are observed. It should be emphasized that the disappearance of the long-range crystalline diffraction peaks of MIL-68(In) does not imply its complete degradation into purely inorganic InO_x clusters. Under the relatively mild solvothermal conditions (120 °C) employed in this study, the complete oxidative decomposition of the organic ligands is thermodynamically unfeasible. Extensive previous studies have demonstrated that the exhaustive transformation of the MIL-68(In) framework into InO_x typically necessitates a high-temperature calcination process strictly exceeding 400 °C [38,39]. Instead of decomposing into inorganic oxides, the MIL-68(In) precursor undergoes an amorphization process. At the same time, XRD diffraction patterns of the intermediate products at different time periods were collected (Fig. S6). The diffraction patterns of the products obtained at 24 h and 48 h were nearly identical, both exhibiting the characteristic diffraction peak of TpBpy, while the intense pristine peaks of MIL-68(In) are virtually absent. This further indicates that the MIL-68(In) MOF undergoes structural dissolution during the synthesis process, resulting in a low content of MIL-68(In) in the composites. The molecular structure and microscopic composition of

the catalysts were analyzed by FT-IR spectroscopy. In contrast to the raw ligands, the stretching vibrations of the C═O and C═C bonds in TpBpy are clearly identified by the prominent bands located at 1610 cm^{-1} and 1560 cm^{-1} (Fig. S7a), respectively, indicating the presence of a keto-enamine structure. Fig. 3b shows that the characteristic peak of MIL-68(In) at 768 cm^{-1} corresponds to the O-In-O stretching vibration. Nevertheless, regardless of whether the composites were synthesized via the in situ solvothermal approach or mechanical mixing, their characteristic infrared absorption bands closely resemble those of pristine TpBpy. This is likely due to the higher content and stronger IR signal of TpBpy relative to MIL-68(In), which makes the characteristic peaks of MIL-68(In) difficult to detect in the composites. Moreover, as shown in Fig. S7b, no obvious characteristic peaks of MIL-68(In) were observed in the composites prepared at reaction times of 24 h and 48 h. As revealed in the enlarged inset of Fig. S7c, a weak characteristic absorption band at approximately 768 cm^{-1} is indeed retained in the TpBpy/20%MIL-68 (In) sample. The continuous presence of this specific O-In-O stretching vibration provides direct structural evidence that the fundamental metal-organic coordination environment is successfully preserved during the dynamic in situ growth.

The optical response of a catalyst significantly affects its solar energy utilization and conversion efficiency during photocatalytic processes. UV–Vis DRS was employed to probe the optical behaviors of the samples. A distinct optical absorption boundary at approximately 450 nm is recorded for MIL-68(In) (Fig. 3c), indicative of its relatively poor light response across the visible spectrum. In contrast to the pristine MOF, the hybrid material displays a substantial optical enhancement in the visible-light range, deriving directly from the superior photosensitizing effect of TpBpy. The bandgaps (E_g) of the catalysts were calculated using the Kubelka-Munk transformation. As shown in Fig. 3d, the bandgaps of MIL-68(In), TpBpy, and TpBpy/20%MIL-68(In) are 2.85 eV, 1.89 eV, and 1.96 eV, respectively. The narrow bandgap of the composite indicates its good optical response, which facilitates the efficient harvesting and utilization of solar energy. N_2 sorption analysis was employed to probe the specific surface areas and the corresponding pore architectures of the as-prepared samples. As shown in Fig. 3e, the N_2 adsorption-desorption isotherms of both TpBpy and TpBpy/20%MIL-68 (In) are of Type IV, indicating the presence of mesoporous structures. TpBpy exhibits a relatively large specific surface area of 641 $m^2 g^{-1}$. The specific surface area of TpBpy/20%MIL-68(In) slightly decreases to 515 $m^2 g^{-1}$, suggesting that MIL-68(In), acting as the precursor, partially alters the local structure of TpBpy. Additionally, as shown in Fig. S8, TpBpy/20%MIL-68(In) displays a pore size distribution similar to that of TpBpy. The thermal robustness of porous organic materials is recognized as a crucial parameter. As depicted in Fig. 3f, MIL-68(In) possesses good thermal stability below 400 °C. Above 400 °C, the framework structure of MIL-68(In) begins to decompose. Meanwhile, the thermal stability of TpBpy/20%MIL-68(In) is similar to that of TpBpy. This is likely because the low content of MIL-68(In) in the composite has no obvious impact on its overall thermal stability.

X-ray photoelectron spectroscopy (XPS) measurements were conducted to investigate the surface elemental composition and the chemical environments of the synthesized samples. The XPS survey spectrum in Fig. S9 indicates the presence of C, N, O, and In elements, thereby confirming the successful preparation of the catalysts. In the high-resolution In 3d spectrum of MIL-68(In), two distinct peaks are observed at binding energies of 453.0 and 445.5 eV, which confirms the presence of the In^{3+} species. (Fig. S10a). Due to the low content of MIL-68(In) in the composite and the uniform loading of TpBpy on the surface, the XPS signal of In in the composite is relatively weak. An argon ion cluster etching technique equipped with the XPS instrument was employed to treat the surface of the composite. As shown in Fig. S10b, the intensity of the In 3d characteristic peaks increases with prolonged etching time, further demonstrating that TpBpy grows on the surface of MIL-68(In) in the composite.

To fundamentally elucidate the interfacial interactions and chemical states within the covalently integrated composite, high-resolution XPS was performed. Compared with pristine TpBpy, the O 1s and N 1s characteristic peaks in the composite both shift towards higher binding energies (Fig. 4c-d). Concurrently, compared with pristine MIL-68(In), the In 3d characteristic peaks in TpBpy/20%MIL-68(In) exhibit a distinct shift to lower binding energies. It is crucial to emphasize that such significant and opposed binding energy shifts cannot be achieved through mere physical contact or electrostatic stacking. Instead, these shifts provide direct and compelling evidence for the profound redistribution of electron cloud density at the interface. By performing in situ irradiated XPS measurements on the argon-ion-cluster-etched TpBpy/20%MIL-68(In) composite, it is found that the In 3d characteristic peaks shift towards higher binding energies after illumination (Fig. 4a), suggesting a reduction in the local electron density around the MIL-68(In) species. However, due to the high content of TpBpy on the surface of the composite, illumination has a minor effect on the peak positions of C, N, and O elements, and no obvious shifts are observed for their characteristic peaks (Fig. 4b-d). The above results illustrate that upon illumination, electrons in the composite tend to transfer from MIL-68(In) to TpBpy, ultimately enabling the highly efficient segregation of photogenerated charge carriers.

3.2. Photocatalytic hydrogen evolution activity

The photocatalytic hydrogen evolution activity of the prepared samples was assessed under full-spectrum illumination. Ascorbic acid and 1 wt% Pt were used as the sacrificial agent and cocatalyst, respectively. As shown in Fig. 5a-b, the hydrogen evolution amount of the catalysts exhibits a steady linear increase over time. Bare MIL-68(In) exhibits negligible photocatalytic activity, which can be primarily ascribed to its limited visible-light absorption capability combined with the fast recombination rate of photogenerated electron-hole pairs. A notable enhancement in H_2 evolution efficiency is recorded for all TpBpy/MIL-68(In) materials formed via the in situ solvothermal route when evaluated against the unmodified TpBpy. Particularly, when the theoretical content of the added MIL-68(In) precursor is 20%, the composite achieves the highest activity of 137 μmol h^{-1} (10 mg catalyst, 13.7 mmol g^{-1} h^{-1}), which is 68.5 and 1.9 times that of pristine MIL-68 (In) and TpBpy, respectively. Meanwhile, as shown in Fig. S11a, the activity of TpBpy/20%MIL-68(In) is notably higher than those of the composite prepared by mechanical mixing and the In-doped TpBpy. The stability of TpBpy/20%MIL-68(In) was systematically evaluated through five continuous recycling experiments. As depicted in Fig. 5c, the high hydrogen production rate can be well maintained simply by supplementing a small amount of sacrificial agent. Furthermore, as observed from Fig. S13 and Fig. S14, the crystal structure, molecular composition, and morphology of the composite exhibit no obvious changes after the cycling tests. To explicitly verify the atomic-level robustness of the local chemical environments, high-resolution XPS was performed on the spent TpBpy/20%MIL-68(In) catalyst after 5 continuous cycles (Fig. S15). Overall, the core characteristic peaks exhibit no noticeable binding energy shifts compared to the fresh catalyst, confirming the exceptional structural stability of the composite framework. It is worth noting that minor peak shifts and slight variations in species proportions are observed in the O 1s and N 1s spectra. These slight changes can be reasonably attributed to the inevitable adsorption of water molecules and dynamic surface interactions during the prolonged photocatalytic water-splitting process in the aqueous solution, rather than any intrinsic degradation of the covalent linkages. This exceptional photocatalytic activity and cycling stability are synergistically governed by the covalently integrated S-scheme heterojunction. Structurally, the dynamic growth mechanism transforms limited two-dimensional physical contact into a three-dimensionally interlocked interface via robust -C═N- covalent bridges. This tight integration not only maximizes the effective contact area and curtails carrier migration paths to construct a high-flux channel for efficient H_2 generation but also

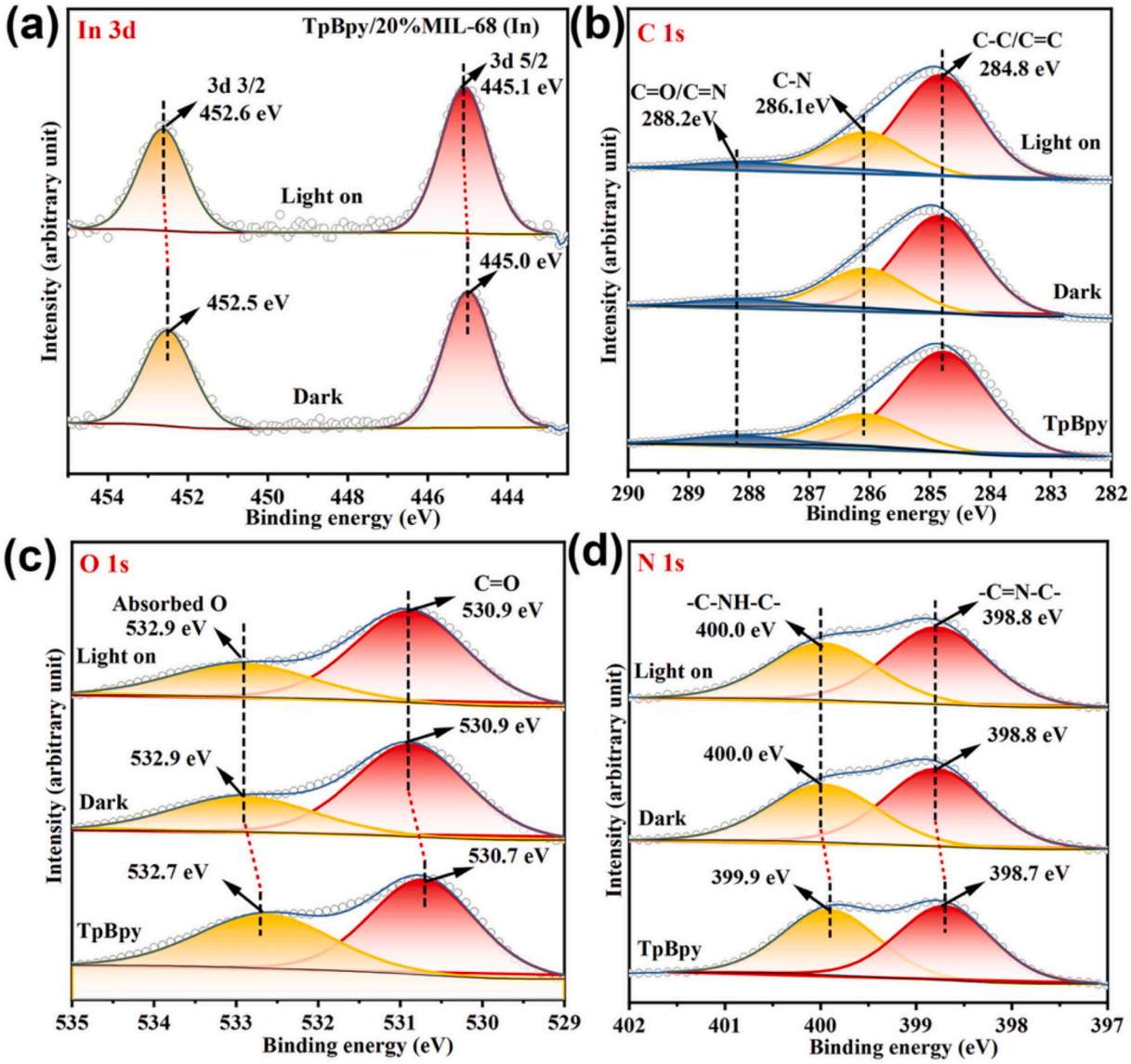

Fig. 4. High-resolution XPS spectra of (a) In 3d, (b) C 1 s, (c) O 1 s, and (d) N 1 s for the TpBpy/MIL-68(In) system.

acts as strong molecular anchors. Unlike physically mixed systems, these covalent linkages effectively pin the MOF and COF phases together, preventing macroscopic phase separation under continuous stirring and prolonged irradiation. Thermodynamically, the directional S-scheme charge transfer pathway acts as a rapid carrier-scavenging mechanism. Driven by the strong internal electric field, the relatively less reductive electrons in the conduction band of MIL-68(In) directly recombine with the less oxidative holes in the valence band of TpBpy. This immediate spatial separation successfully preserves the highly reactive electrons for proton reduction, while allowing the highly oxidative holes in the valence band of MIL-68(In) to be swiftly consumed by the sacrificial agent. Ultimately, this directional transfer prevents the detrimental accumulation of unreacted carriers, fundamentally boosting the overall H_2 generation efficiency and protecting the porous frameworks from self-oxidation (photocorrosion) during long-term redox cycles.

To systematically evaluate its catalytic standing, the TpBpy/20% MIL-68(In) composite is assessed alongside several reference MOF-based and COF-based systems. As summarized in Table S1, the optimal TpBpy/20%MIL-68(In) composite delivers an exceptional H_2 generation rate of 13.7 mmol g^{-1} h^{-1}. This performance outperforms recently reported MOF/COF S-scheme heterojunctions, such as MOF-808@TpPa-1-COF (11.88 mmol g^{-1} h^{-1}) [40] and DHU-COF-BB (12.8 mmol g^{-1} h^{-1}) [41]. Furthermore, the effect of sacrificial agent types on the catalytic activity was investigated. Among the evaluated candidates, ascorbic acid emerges as the most highly efficient sacrificial electron donor for the current photocatalytic setup (Fig. S11b). Meanwhile, the hydrogen evolution amount under different catalyst dosages was evaluated (Fig. S12). The results indicate that when the catalyst dosage is less than 10 mg, the hydrogen evolution amount exhibits a linear increase with the dosage. Upon elevating the catalyst loading to 20 mg, the upward trend in the H_2 evolution rate begins to decelerate. When the dosage continues to increase to 50 mg, the hydrogen evolution amount decreases instead. This is primarily because an excessive amount of catalyst induces a light-shielding effect, which reduces the absorption efficiency of the photocatalytic system for simulated solar light. Therefore, 10 mg was selected as the optimal catalyst dosage for the hydrogen evolution activity tests. To evaluate the utilization and conversion efficiency of solar energy by the photocatalytic system, the AQE of the TpBpy/20%MIL-68(In) composite under irradiation with different wavelengths was measured. As presented in Fig. 5d and Table S2, the variation trend of the AQE is consistent with the light absorption curve of the material, indicating that the illumination condition is a vital factor influencing the catalyst activity. The composite achieves a maximum AQE of 0.85% under irradiation at a wavelength of 420 nm.

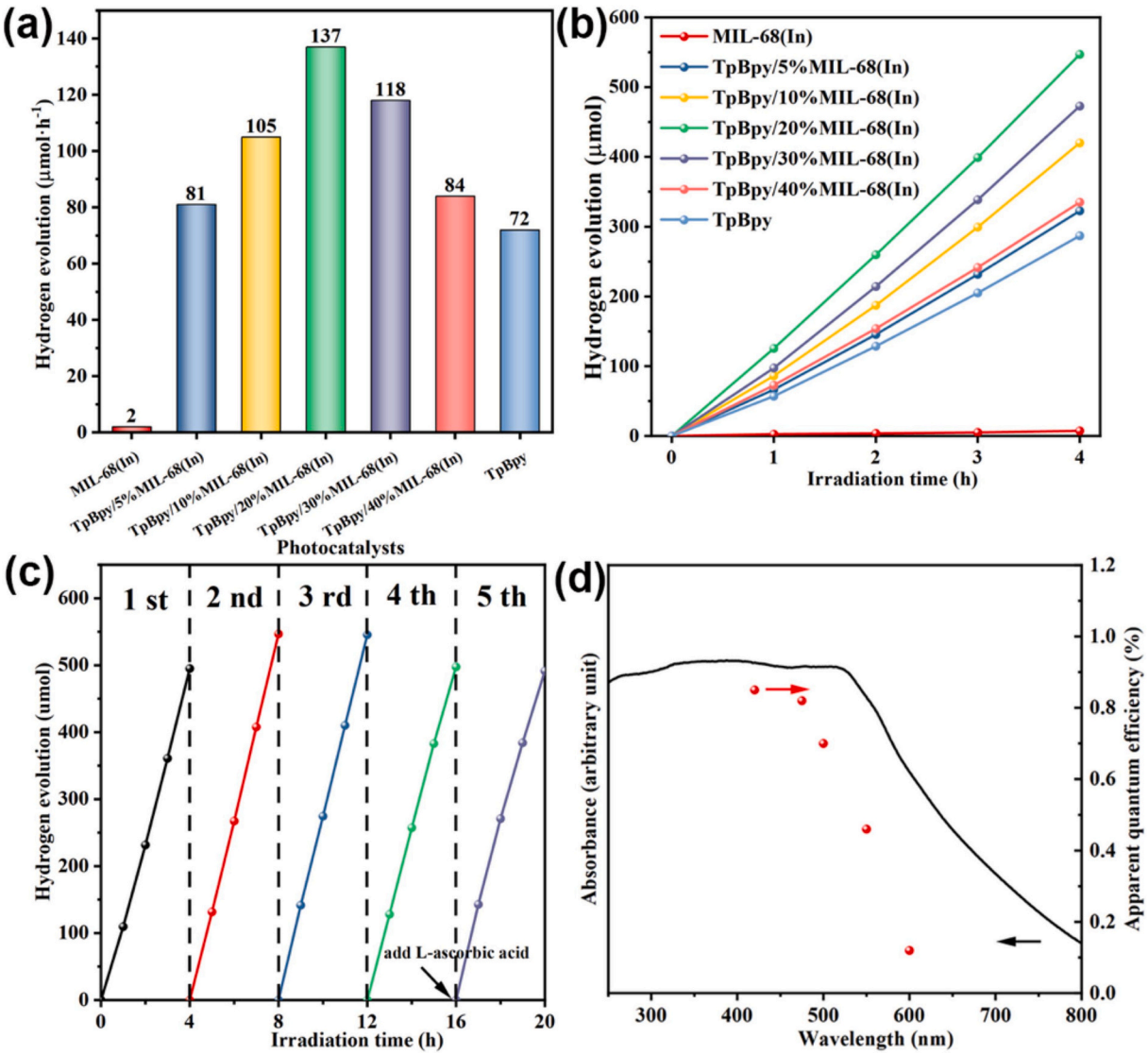

Fig. 5. (a) Photocatalytic hydrogen evolution rates and (b) time-yield plots of the prepared samples; (c) Cycling stability of TpBpy/20%MIL-68(In) over five runs; (d) Wavelength-dependent apparent quantum efficiency (AQE) alongside the UV–Vis absorption spectrum of TpBpy/20%MIL-68(In).

3.3. Photoelectrochemical property characterization

To elucidate the charge migration kinetics, which fundamentally dictates the photocatalytic capability, the photoelectrochemical behaviors of the heterostructures were systematically evaluated. Fig. 6a shows that pristine MIL-68(In) generates a negligible photocurrent signal, a finding that aligns well with its poor photocatalytic hydrogen evolution performance. Meanwhile, compared with pristine TpBpy, the transient photocurrent intensity of the TpBpy/20%MIL-68(In) composite is significantly enhanced, indicating a higher migration efficiency of photogenerated electrons within the composite [42,43].

Furthermore, the electrochemical impedance of the catalysts was measured, and an equivalent circuit model was established. The results are presented in Fig. 6b and Table S3. In this equivalent circuit model, R_s and R_{ct} denote the uncompensated electrolyte solution resistance and the interfacial charge-transfer resistance, respectively. Meanwhile, CPE accounts for the double-layer capacitance, and Z_w corresponds to the Warburg diffusion impedance. Relative to the pristine counterparts, the optimal TpBpy/20%MIL-68(In) heterostructure presents a noticeably contracted Nyquist arc, which signifies a diminished interfacial charge-transfer resistance (R_{ct}). This observation robustly substantiates the accelerated transport and superior dissociation dynamics of the photogenerated electron-hole pairs within the hybrid matrix. From the steady-state photoluminescence (PL) spectra of the catalysts (Fig. 6c), the results reveal that the PL intensity of the TpBpy/20%MIL-68(In) composite is remarkably decreased compared to that of pristine TpBpy, revealing a significantly inhibited recombination process of the photogenerated electron-hole pairs in the heterostructure. Concurrently, the composite possesses a longer time-resolved PL decay lifetime (Fig. 6d), further confirming the higher migration efficiency of internal photogenerated charges. In summary, the small amount of MIL-68(In) in the TpBpy/20%MIL-68(In) composite is tightly integrated with TpBpy to form a heterojunction. This architecture facilitates the robust spatial decoupling of photogenerated electron-hole pairs, consequently accelerating charge transport kinetics and boosting the ultimate hydrogen evolution performance. Furthermore, by employing TEMPO as a specific electron scavenger, the electron spin resonance (ESR) signals of the TpBpy/20%MIL-68(In) composite were measured, with the results shown in Fig. S16. Upon exposure to simulated solar illumination, the ESR signal of the material is noticeably weakened. This is due to the trapping of electrons by TEMPO, which leads to a decrease in its generated signal, further indicating that the composite produces a large amount of photogenerated electrons under illumination conditions.

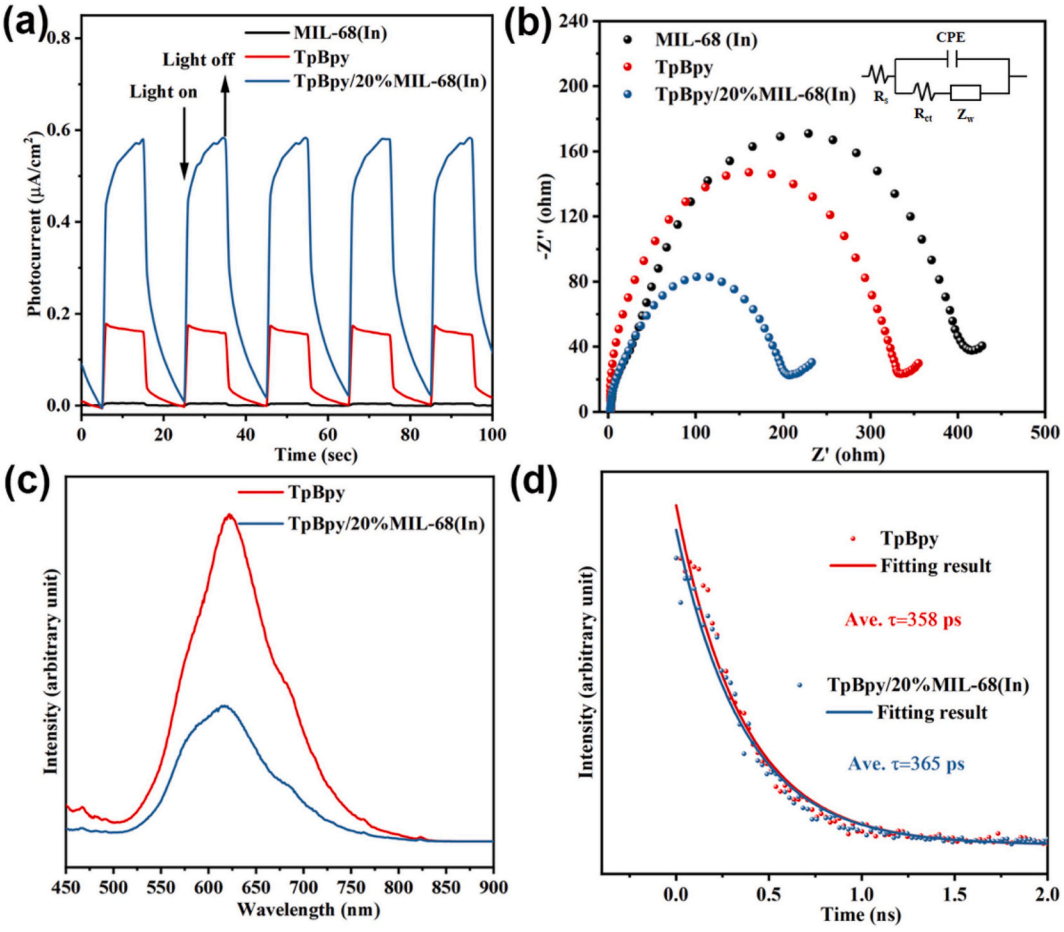

Fig. 6. Transient photocurrent (a), EIS Nyquist plots (b), photoluminescence spectra (c) and time-resolved photoluminescence spectra (d) of TpBpy/MIL-68 (In) system.

3.4. Photocatalytic mechanism

The energy band structure of each component in the composite has a significant impact on its photocatalytic reaction mechanism. Therefore, the band positions of the catalysts were analyzed using Mott-Schottky plots in this study. Fig. 7a-c shows that, using an Ag/AgCl electrode as the reference, the flat-band potentials (E_{FB}) of MIL-68(In), TpBpy, and TpBpy/20%MIL-68(In) are measured to be −0.70 V, −0.99 V, and −0.90 V, respectively. Furthermore, the positive gradients observed in the Mott-Schottky curves reveal the n-type semiconducting nature of all three evaluated materials. Typically, the conduction band minimum (E_{CB}) of an n-type semiconductor is positioned roughly 0.20 V more negative than its corresponding flat-band potential. Concurrently, the potential difference between the normal hydrogen electrode (NHE) and the Ag/AgCl electrode is about 0.20 V. Consequently, the conduction band potentials (E_{CB}) for bare MIL-68(In), pristine TpBpy, and the TpBpy/20%MIL-68(In) composite are established as −0.70, −0.99, and − 0.90 eV (vs. NHE), respectively. By coupling these values with the optical bandgaps derived from the UV–Vis DRS profiles ($E_g = E_{VB} - E_{CB}$), the corresponding valence band (E_{VB}) positions are deduced to be 2.15, 0.90, and 1.06 eV. Integrating the preceding findings, the energy band structures of the catalysts can be clearly obtained, as depicted in Fig. 7d. The energy band distributions of MIL-68(In) and TpBpy satisfy the formation conditions for an S-scheme heterojunction [44].

Density functional theory (DFT) calculations were performed to further elucidate the charge transfer mechanism and the photocatalytic reaction mechanisms of the catalysts. As shown in Fig. 8a-c, the structural models for hydrogen adsorption on MIL-68(In), TpBpy, and TpBpy/20%MIL-68(In) were constructed, and the corresponding hydrogen adsorption free energies (ΔG) were calculated. It should be noted that in this synergistic photocatalytic system, while the loaded Pt nanoparticles act as the terminal reactive sites for H_2 generation, the semiconductor support plays a crucial preceding role in proton activation. The ΔG on the models is intended to evaluate the intrinsic thermodynamic evolution of the support driven by the heterojunction formation. As observed from Fig. 8d, compared with the individual components, the ΔG of the composite is significantly optimized and closer to the ideal value of zero. This indicates that the S-scheme covalent integration profoundly modulates the surface electronic structure, transforming the TpBpy surface into an efficient proton-enrichment platform. This intrinsically optimized micro-environment strongly facilitates the initial pre-adsorption of protons and accelerates their subsequent transfer to the adjacent Pt cocatalyst, thereby collectively boosting the overall hydrogen evolution kinetics. It is worth mentioning that the subsequent specific dynamic transfer of these enriched protons from the platform to the Pt sites is a complex kinetic process. In an actual aqueous system, this transfer inevitably involves complex solvent effects and solid-liquid interfacial diffusion. The exact calculation of this dynamic energy barrier requires advanced explicit solvation models and molecular dynamics, which presents a highly valuable direction for future in-depth theoretical investigations.

Furthermore, theoretical calculations were performed to evaluate the work functions of the materials. As depicted in Fig. 9a-b, the calculated values for MIL-68(In) and TpBpy are determined to be 5.93 eV and 5.46 eV, respectively. As expressed by the following equation: Fermi level = vacuum level - work function, TpBpy possesses a smaller

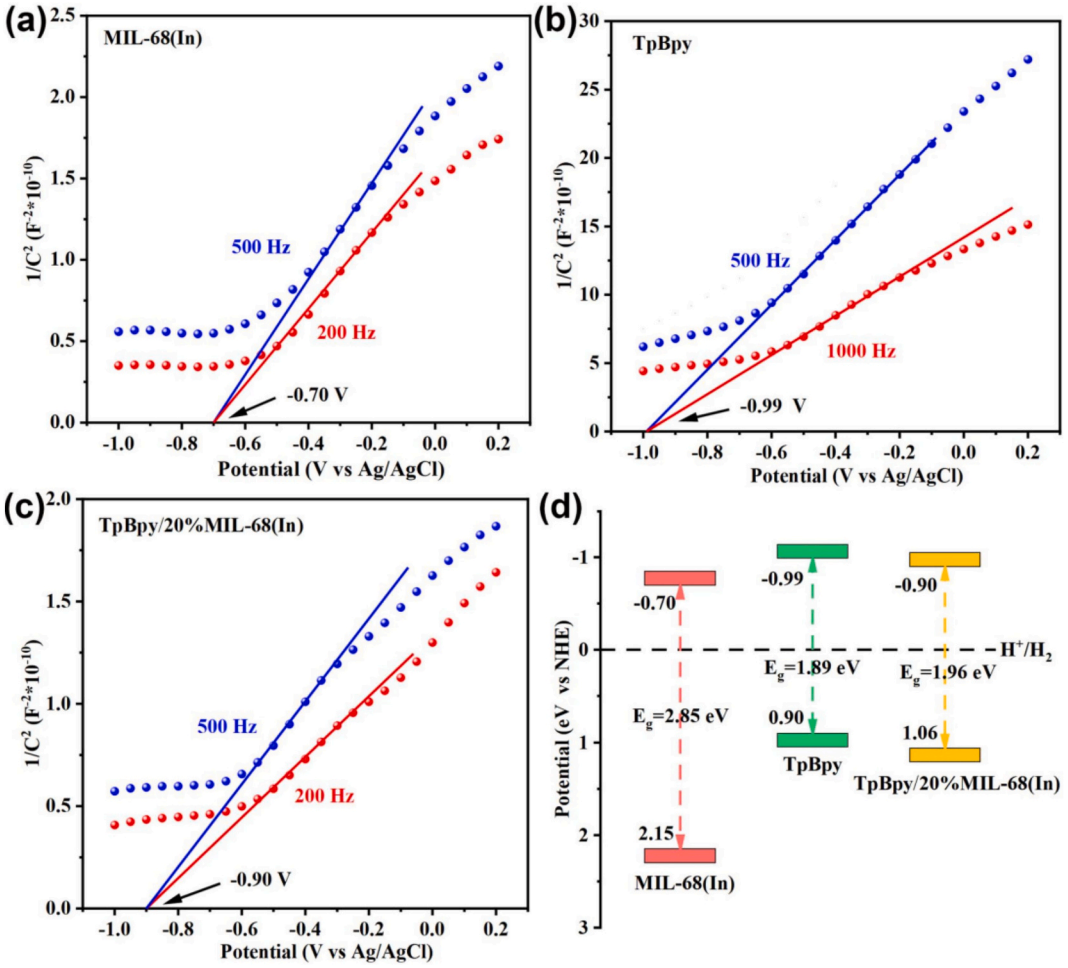

Fig. 7. Mott-Schottky plots of MIL-68(In) (a), TpBpy (b) and TpBpy/20%MIL-68(In) (c), schematic illustration of band positions for TpBpy/MIL-68(In) system.

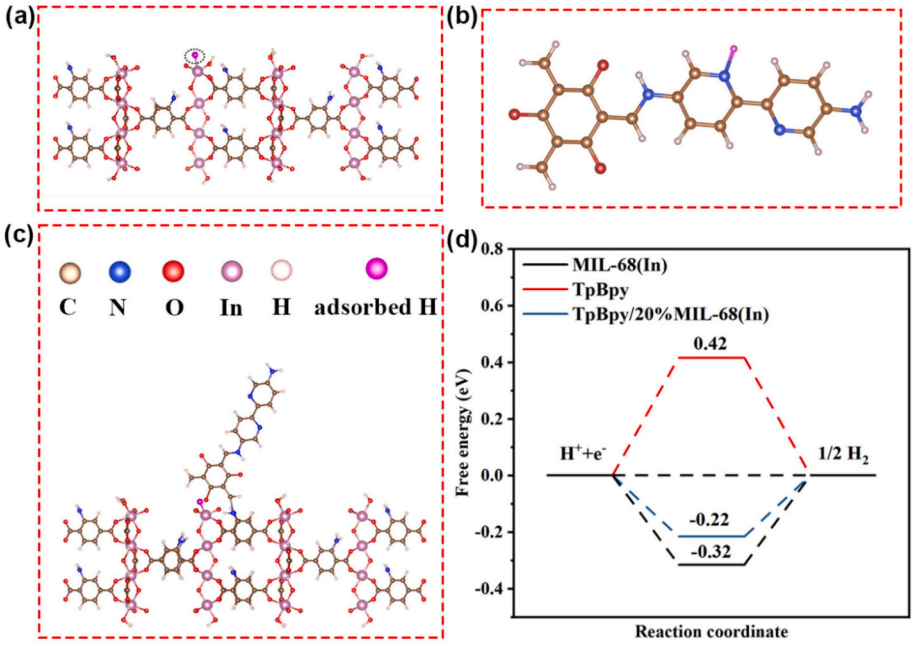

Fig. 8. (a-c) Schematic structure models of H adsorption site of the catalysts, (d) free energy diagrams of reaction on the catalysts.

work function and consequently a higher Fermi level. When TpBpy is tightly integrated with MIL-68(In) via covalent bonding, a strong

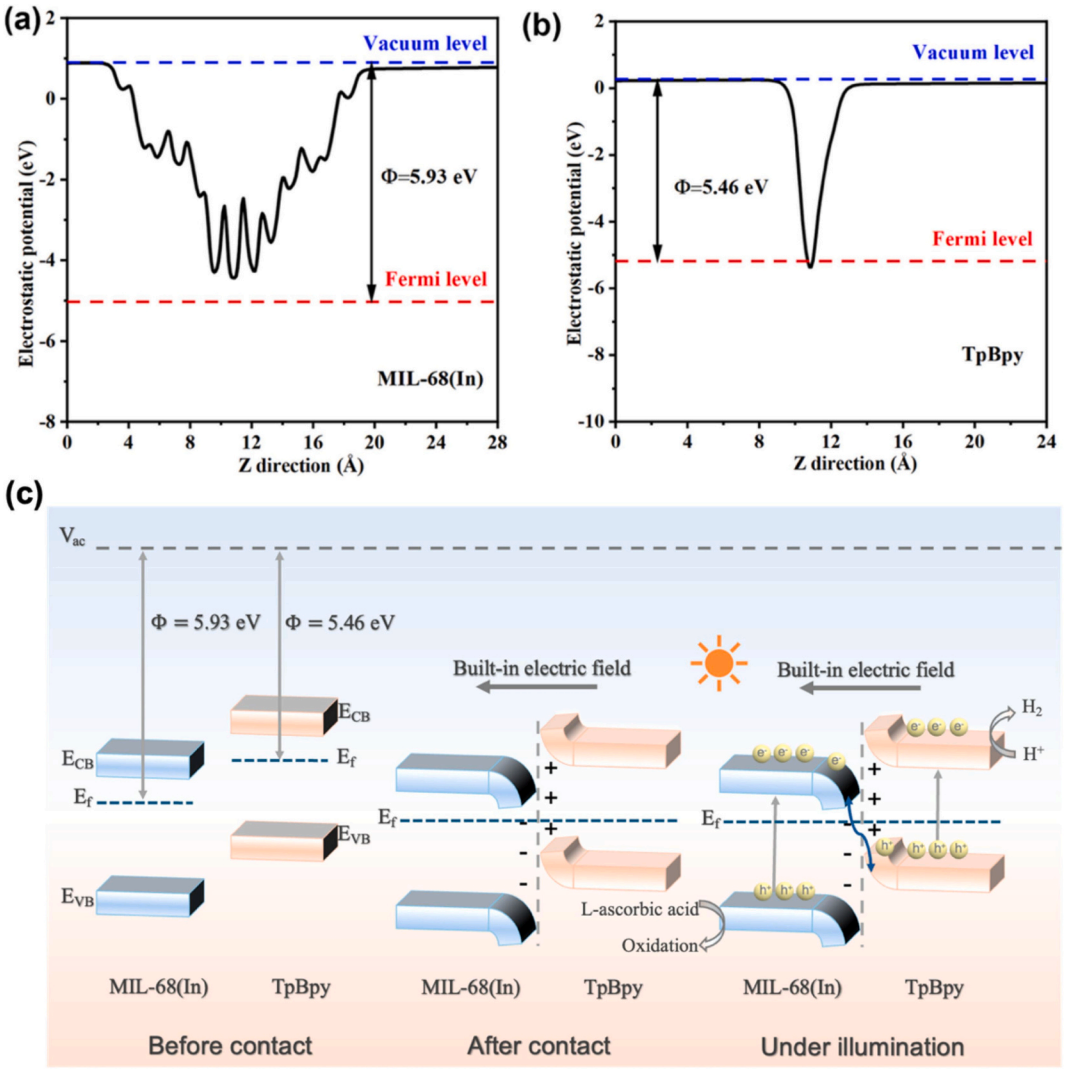

Fig. 9. (a-b) Electrostatic potentials of the catalysts, (c) schematic illustration of photocatalytic reaction mechanism for TpBpy/MIL-68(In).

interfacial interaction is generated. Their Fermi levels tend to equilibrate, driving electrons to transfer from TpBpy to MIL-68(In). Meanwhile, the calculated charge density difference (Fig. S17) indicates that the electrons in the composite tend to accumulate on the MIL-68(In) side. Consequently, the energy bands of MIL-68(In) bend downward while those of TpBpy bend upward, establishing a strong internal electric field (IEF) directed from TpBpy to MIL-68(In) at the interface. Under light irradiation, the possibility of a conventional Type-II charge transfer pathway can be reasonably ruled out based on the in situ irradiated XPS data and band position analysis. In a typical Type-II heterojunction, photogenerated electrons would migrate from the more negative conduction band (CB) of TpBpy (−0.99 V vs. NHE) to the CB of MIL-68(In) (−0.70 V vs. NHE). If this pathway were dominant, the electron density on the MIL-68(In) side would increase during continuous irradiation. However, the in situ light irradiated XPS spectra reveal that the In 3d characteristic peaks of MIL-68(In) shift to higher binding energies under illumination, suggesting a quantifiable decrease in local electron density. This experimental observation strongly supports the proposed S-scheme photocatalytic mechanism (Fig. 9c). Driven by the IEF and band bending, the relatively less reductive photogenerated electrons in the CB of MIL-68(In) are propelled across the covalent interface to recombine with the holes in the VB of TpBpy. Consequently, the powerful reducing electrons in the CB of TpBpy and the highly oxidative holes in the VB of MIL-68(In) are spatially separated and successfully preserved. This allows an abundance of highly reactive electrons to accumulate in the conduction band of TpBpy, thereby thermodynamically triggering the reduction of aqueous protons (H^+) into hydrogen (H_2). The covalently connected TpBpy/MIL-68(In) S-scheme heterojunction not only provides a rapid channel for electron transfer [45,46], but also accelerates the transfer kinetics and dissociation of photogenerated carriers, which directly translates into an augmented capacity for photocatalytic hydrogen generation.

4. Conclusion

Overall, a novel S-scheme heterostructure based on covalently integrated TpBpy/MIL-68(In) was constructed via an in situ solvothermal method. This covalent S-scheme heterojunction successfully addresses the intrinsic drawbacks of both single components. Specifically, the TpBpy framework mitigates the limited visible-light absorption of MIL-68(In), while the exposed metal nodes, low-impedance covalent channels, and built-in electric field drive an efficient directional charge transfer that simultaneously overcomes the lack of active sites, poor conductivity, and severe carrier recombination. Consequently, the optimal TpBpy/20%MIL-68(In) composite exhibits highly efficient photocatalytic performance, delivering a H_2 generation rate of 13.7 mmol g^{-1} h^{-1}, which is 68.5 and 1.9 times that of pristine MIL-68(In) and TpBpy, respectively. More importantly, comprehensive analysis

combining XPS binding energy shifts and DFT calculations provides solid evidence of interfacial electron cloud redistribution. The results confirm at the atomic and energy-level scales that these covalent bridges create low-impedance pathways and a strong internal electric field (IEF). This effectively overcomes the high contact resistance inherent to physically mixed systems, thereby driving a highly efficient directional charge flow and spatial segregation of photogenerated carriers via an S-scheme heterojunction mode. This work highlights the potential of covalent interfacial engineering in MOF/COF systems, offering new strategies for developing low-cost and stable porous organic/inorganic composite photocatalysts for solar energy conversion.

CRediT authorship contribution statement

Yuying Hu: Writing – original draft, Validation, Investigation. **Huihui Zhang:** Methodology, Conceptualization. **Jiayi Meng:** Writing – review & editing. **Yifan Liao:** Data curation. **Yuchen Wei:** Formal analysis. **Quanmei Zhou:** Validation. **Mohan Zhang:** Formal analysis. **Yamei Huang:** Validation. **Wei-Lin Dai:** Writing – review & editing, Visualization, Supervision, Project administration, Funding acquisition.

Declaration of competing interest

The authors declare that they have no conflicts of interest.

Acknowledgments

This work was funded by the National Key Research and Development Program of China (2021YFA1501404), and the Science and Technology Commission of Shanghai Municipality (2024ZDSYS02).

Appendix A. Supplementary data

Supplementary data to this article can be found online at https://doi.org/10.1016/j.cej.2026.179707.

Data availability

Data will be made available on request.

References

[1] Y. Yang, C. Zhang, C. Lai, G. Zeng, D. Huang, M. Cheng, J. Wang, F. Chen, C. Zhou, W. Xiong, BiOX (X = Cl, Br, I) photocatalytic nanomaterials: applications for fuels and environmental management, Adv. Colloid Interf. Sci. 254 (2018) 76–93, https://doi.org/10.1016/j.cis.2018.03.004.

[2] S. Cao, J. Low, J. Yu, M. Jaroniec, Polymeric photocatalysts based on graphitic carbon nitride, Adv. Mater. 27 (2015) 2150–2176, https://doi.org/10.1002/adma.201500033.

[3] C.I. Yeo, Y.S. Tan, H.T.A. Awan, A. Hanan, W.P. Wong, R. Walvekar, B.H. Goh, M. Khalid, A review on the advancements in covalent organic frameworks for photocatalytic reduction of carbon dioxide, Coord. Chem. Rev. 521 (2024) 216167, https://doi.org/10.1016/j.ccr.2024.216167.

[4] S.E. Hosseini, M.A. Wahid, Hydrogen production from renewable and sustainable energy resources: promising green energy carrier for clean development, Renew. Sust. Energ. Rev. 57 (2016) 850–866, https://doi.org/10.1016/j.rser.2015.12.112.

[5] J. Pan, D. Wang, B. Zhang, C. Zhao, D. Liu, S. Liu, Z. Zeng, T. Chen, G. Liu, S. Jiao, Z. Xu, T. Liu, T. Liu, X. Fang, L. Zhao, J. Wang, Atomic-level charge separation boosting the photocatalytic hydrogen evolution, Chem. Eng. J. 487 (2024) 150536, https://doi.org/10.1016/j.cej.2024.150536.

[6] M. Cao, F. Yang, Q. Zhang, J. Zhang, L. Zhang, L. Li, X. Wang, W. Dai, Facile construction of highly efficient MOF-based Pd@UiO-66-NH_2@$ZnIn_2S_4$ flower-like nanocomposites for visible-light-driven photocatalytic hydrogen production, J. Mater. Sci. Technol. 76 (2021) 189–199, https://doi.org/10.1016/j.jmst.2020.11.028.

[7] C.H. Liao, C.W. Huang, J.C.S. Wu, Hydrogen production from semiconductor-based photocatalysis via water splitting, Catalysts 2 (2012) 490–516, https://doi.org/10.3390/catal2040490.

[8] H. Zhong, S. Chen, Z. Jiang, J. Hu, J. Dong, L.H. Chung, Q.C. Lin, W. Ou, L. Yu, J. He, Utilizing metal-thiocatecholate functionalized UiO-66 framework for photocatalytic hydrogen evolution reaction, Small 19 (2023) 2207266, https://doi.org/10.1002/smll.202207266.

[9] M.A. Rehan, H. Liang, G. Li, Synergistic role of plasmonic Au-doped MOF with $ZnIn_2S_4$/MoS_2 nanosheets for boosted photocatalytic hydrogen evolution, Nano Mater. Sci. (2024), https://doi.org/10.1016/j.nanoms.2024.06.001.

[10] Z. Abou Khalil, R. Del Angel, G. Mouchaham, C. Serre, M. Daturi, M. El-Roz, Photocatalytic water splitting reaction: the pathway from semiconductors to MOFs, J. Photochem. Photobiol. C Photchem. Rev. 60-61 (2024) 100680, https://doi.org/10.1016/j.jphotochemrev.2024.100680.

[11] S. Bao, Q. Tan, S. Wang, J. Guo, K. Lv, S.A.C. Carabineiro, L. Wen, TpBD COF@$ZnIn_2S_4$ nanosheets: a novel S-scheme heterojunction with enhanced photoreactivity for hydrogen production, Appl. Catal. B Environ. 330 (2023) 122624, https://doi.org/10.1016/j.apcatb.2023.122624.

[12] H. Zhang, Z. Lin, P. Kidkhunthod, J. Guo, Stable immobilization of nickel ions on covalent organic frameworks for panchromatic photocatalytic hydrogen evolution, Angew. Chem. Int. Ed. 62 (2023) e202217527, https://doi.org/10.1002/anie.202217527.

[13] Z. Li, T. Deng, S. Ma, Z. Zhang, G. Wu, J. Wang, Q. Li, H. Xia, S. Yang, X. Liu, Three-component donor-π-acceptor covalent-organic frameworks for boosting photocatalytic hydrogen evolution, J. Am. Chem. Soc. 145 (2023) 8364–8374, https://doi.org/10.1021/jacs.2c11893.

[14] Q. Zhou, Y. Wei, Y. Liao, J. Meng, Y. Huang, X. Wang, H. Zhang, W. Dai, Recent studies on the construction of MOF-based composites and their applications in photocatalytic hydrogen evolution, Molecules 30 (2025) 2755, https://doi.org/10.3390/molecules30132755.

[15] A. Dhakshinamoorthy, Z. Li, S. Yang, H. Garcia, Metal-organic framework heterojunctions for photocatalysis, Chem. Soc. Rev. 53 (2024) 3002–3035, https://doi.org/10.1039/D3CS00205E.

[16] J. Li, H. Chang, S. Feng, H. Jian, Q. Shen, X. Liu, H. Jia, J. Xue, TiO_2@Ti MOFs hollow double-shell structure by in-situ self-sacrificial hydrolytic etching for enhanced photocatalytic hydrogen evolution, Chem. Eng. J. 498 (2024) 155542, https://doi.org/10.1016/j.cej.2024.155542.

[17] L. Liu, L. Zuo, X. Zhai, X. Xiao, H. Fan, B. Li, L. Wang, A novel hexagonal prism of Zr-based MOF@$ZnIn_2S_4$ core-shell nanorod as an efficient photocatalyst for hydrogen evolution, Appl. Catal. B Environ. 361 (2025) 124686, https://doi.org/10.1016/j.apcatb.2024.124686.

[18] J. Ye, Z. Fan, B. Hu, Y. Xie, Y. Ling, Y. Wang, Ni-MOFs/$ZnIn_2S_4$ organic-inorganic hybrid materials enhancement photocatalytic hydrogen evolution under visible light via faster carrier separation efficiency, Fuel 380 (2025) 133271, https://doi.org/10.1016/j.fuel.2024.133271.

[19] K. Wang, S. Liu, P. Zhu, M. Yang, Z. Jin, Rational design of a novel S-scheme heterojunction based on ZIF-67-supported Ni-Fe layered double hydroxide for efficient photocatalytic hydrogen generation, Energy Fuel 36 (2022) 2058–2067, https://doi.org/10.1021/acs.energyfuels.1c04180.

[20] R. Shen, X. Li, C. Qin, P. Zhang, X. Li, Efficient photocatalytic hydrogen evolution by modulating excitonic effects in Ni-intercalated covalent organic frameworks, Adv. Energy Mater. 13 (2023) 2203695, https://doi.org/10.1002/aenm.202203695.

[21] R. Shen, G. Liang, L. Hao, P. Zhang, X. Li, In situ synthesis of chemically bonded 2D/2D covalent organic frameworks/O-vacancy WO_3 Z-scheme heterostructure for photocatalytic overall water splitting, Adv. Mater. 35 (2023) 2303649, https://doi.org/10.1002/adma.202303649.

[22] M. Lu, S. Zhang, M. Yang, Y. Liu, J. Liao, P. Huang, M. Zhang, S. Li, Z. Su, Y. Lan, Dual photosensitizer coupled three-dimensional metal-covalent organic frameworks for efficient photocatalytic reactions, Angew. Chem. Int. Ed. 62 (2023) e202307632, https://doi.org/10.1002/anie.202307632.

[23] M. Xu, M. Lu, G. Qin, X. Wu, T. Yu, L. Zhang, K. Li, X. Cheng, Y. Lan, Piezo-photocatalytic synergy in $BiFeO_3$@COF Z-scheme heterostructures for high-efficiency overall water splitting, Angew. Chem. Int. Ed. 61 (2022) e202210700, https://doi.org/10.1002/anie.202210700.

[24] Y. Zhang, Y. Huang, X. Wang, H. Zhang, L. Gao, Y. Li, Y. Liao, J. Meng, Y. Cui, Z. Li, W. Dai, Interface interaction modulates charge transfer in flower-like In_2S_3 nanosheets/COF composite for efficient solar-to-H_2O_2 conversion, Sep. Purif. Technol. 358 (2025) 130374, https://doi.org/10.1016/j.seppur.2024.130374.

[25] L. Wang, J. Mao, G. Huang, Y. Zhang, J. Huang, H. She, C. Liu, H. Liu, Q. Wang, Configuration of hetero-framework via integrating MOF and triazine-containing COF for charge-transfer promotion in photocatalytic CO_2 reduction, Chem. Eng. J. 446 (2022) 137011, https://doi.org/10.1016/j.cej.2022.137011.

[26] F. Zhang, J. Sheng, Z. Yang, X. Sun, H. Tang, M. Lu, H. Dong, F. Shen, J. Liu, Y. Lan, Rational design of MOF/COF hybrid materials for photocatalytic H_2 evolution in the presence of sacrificial electron donors, Angew. Chem. Int. Ed. 57 (2018) 12106–12110, https://doi.org/10.1002/anie.201806862.

[27] J. Low, J. Yu, M. Jaroniec, S. Wageh, A.A. Al-Ghamdi, Heterojunction photocatalysts, Adv. Mater. 29 (2017) 1601694, https://doi.org/10.1002/adma.201601694.

[28] B. Zhu, J. Sun, Y. Zhao, L. Zhang, J. Yu, Construction of 2D S-scheme heterojunction photocatalyst, Adv. Mater. 36 (2024) 2310600, https://doi.org/10.1002/adma.202310600.

[29] H. Liu, M. Yan, Z. Wang, G. Xie, X. Pu, Y. Fu, X. Peng, H. Wang, J. Wang, Constructing boosted charge separation for efficient H_2O_2 production and pollutant degradation by highly defective $ZnIn_2S_4$/carbon doped boron nitride, J. Environ. Chem. Eng. 12 (2024) 114251, https://doi.org/10.1016/j.jece.2024.114251.

[30] E.S. Ghalehsefíd, Z.G. Jahani, A. Aliabadi, M. Ghodrati, A. Khamesan, A. ParsaeiKhomami, M. Mousavi, M.-A. Hosseini, J.B. Ghasemi, X. Li, TiO_2 nanotube/$ZnIn_2S_4$ nanoflower composite with step-scheme heterojunction for efficient photocatalytic H_2O_2 production and organic dye degradation, J. Environ. Chem. Eng. 11 (2023) 110160, https://doi.org/10.1016/j.jece.2023.110160.

[31] X. Zeng, Y. Liu, Y. Kang, Q. Li, Y. Xia, Y. Zhu, H. Hou, M. Uddin, T. Gengenbach, D. Xia, C. Sun, D. McCarthy, A. Deletic, J. Yu, X. Zhang, Simultaneously tuning charge separation and oxygen reduction pathway on graphitic carbon nitride by polyethylenimine for boosted photocatalytic hydrogen peroxide production, ACS Catal. 10 (2020) 3697–3706, https://doi.org/10.1021/acscatal.9b05247.
[32] W. Li, G. Zuo, S. Ma, L. Xi, C. Ouyang, M. He, Y. Wang, Q. Ji, S. Yang, W. Zhu, K. Zhang, H. He, Localized photothermal effect mediated hollow S-scheme $NiCo_2O_4$@$ZnIn_2S_4$ for enhanced photocatalytic hydrogen evolution, Appl. Catal. B Environ. 365 (2025) 124971, https://doi.org/10.1016/j.apcatb.2024.124971.
[33] T.F. Qahtan, T.O. Owolabi, O.E. Olubi, A. Hezam, Emerging tandem S-scheme heterojunction photocatalysts, Coord. Chem. Rev. 514 (2024) 215839, https://doi.org/10.1016/j.ccr.2024.215839.
[34] Y. Qiu, C. Jiang, X. Xin, Y.-Y. Li, H. Wang, J. Xu, H. Lin, L. Wang, V. Turkevich, Site-specified MOF/COF heteronanosheets for enhancing photocatalytic CO_2 reduction, ACS Appl. Nano Mater. 7 (2024) 11234–11247, https://doi.org/10.1021/acsanm.4c00764.
[35] J. Cheng, W. Wang, S. Cao, Y. Lan, Covalent organic framework-based heterojunction photocatalysts, Natl. Sci. Rev 12 (2025), https://doi.org/10.1093/nsr/nwaf462 nwaf462.
[36] G. Yuan, L. Tan, P. Wang, Y. Wang, C. Wang, H. Yan, Y.-Y. Wang, MOF-COF composite photocatalysts: design, synthesis, and mechanism, Cryst. Growth Des. 22 (2021) 893–908, https://doi.org/10.1021/acs.cgd.1c01071.
[37] T. Yang, B. Wang, P.K. Chu, J. Xia, Self-sacrificing MOF-derived hierarchical porous In_2S_3 nanostructures with enhanced photocatalytic performance, Chin. J. Catal. 59 (2024) 204–213, https://doi.org/10.1016/S1872-2067(24)60003-3.
[38] D. Arif, Z. Hussain, A.D. Abbasi, M. Sohail, Ag functionalized In_2O_3 derived from MIL-68(in) as an efficient electrochemical glucose sensor, Front. Chem. 10 (2022) 906031, https://doi.org/10.3389/fchem.2022.906031.
[39] X. Wang, F. Gu, Z. Wang, MOF-derived Pr-doped In_2O_3 hollow tubes rich in oxygen vacancies for enhancing the n-butanol sensing performance, J. Mater. Chem. C 13 (2025) 9724–9735, https://doi.org/10.1039/d5tc00781j.
[40] H. Zhang, Y. Yang, C. Li, H. Tang, F. Zhang, G. Zhang, H. Yan, A new strategy for constructing covalently connected MOF@COF core-shell heterostructures for enhanced photocatalytic hydrogen evolution, J. Mater. Chem. A 9 (2021) 16743–16750, https://doi.org/10.1039/D1TA04493A.
[41] Y. Huang, B. Gao, Q. Huang, D.L. Ma, H. Wu, C. Qian, Constructing benzothiadiazole-based donor-acceptor covalent organic frameworks for efficient photocatalytic H_2 evolution, Aggregate 6 (2024) e669, https://doi.org/10.1002/agt2.669.
[42] C. Jiang, Y. Qiu, X. Xin, Y. Li, H. Li, H. Wang, J. Xu, H. Lin, L. Wang, V. Turkevych, MOF-templated tubular $Ni_{1-x}Co_xS_2$-CdS heterojunction with intensified direct Z-scheme charge transmission for highly promoted visible-light photocatalysis, Nano Res. 17 (2024) 6281–6293, https://doi.org/10.1007/s12274-024-6636-z.
[43] G. Zhang, M. Zhao, L. Su, H. Yu, C. Wang, D. Sun, Y. Ding, Donor-acceptor covalent-organic frameworks based on phthalimide as an electron-deficient unit for efficient visible-light catalytic hydrogen evolution, ACS Appl. Mater. Interfaces 15 (2023) 20310–20316, https://doi.org/10.1021/acsami.3c00786.
[44] W. Dong, Y. Xiao, Z. Qin, B. Qiao, L. Li, Partially H-bonded covalent organic frameworks for photocatalytic hydrogen evolution, J. Mater. Chem. A 11 (2023) 14760, https://doi.org/10.1039/D3TA01944F.
[45] Q. Xu, L. Zhang, B. Cheng, J. Fan, J. Yu, S-scheme heterojunction photocatalyst, Chem 6 (2020) 1543–1559, https://doi.org/10.1016/j.chempr.2020.06.010.
[46] C. Cheng, J. Zhang, B. Zhu, G. Liang, L. Zhang, J. Yu, Verifying the charge-transfer mechanism in S-scheme heterojunctions using femtosecond transient absorption spectroscopy, Angew. Chem. Int. Ed. 62 (2023) e202218688, https://doi.org/10.1002/anie.202218688.